Fast and slow timescales in the tropical low-cloud response to increasing CO_2 in two climate models

Masahiro Watanabe[1], Hideo Shiogama[2], Masakazu Yoshimori[1], Tomoo Ogura[2], Tokuta Yokohata[2], Hajime Okamoto[3], Seita Emori[1,2], and Masahide Kimoto[1]

1: Atmosphere and Ocean Research Institute, the University of Tokyo
2: National Institute for Environmental Studies
3: Research Institute for Applied Mechanics, Kyushu University

Submitted to *Climate Dynamics*

June 1, 2011

Corresponding author:
M. Watanabe, Atmosphere and Ocean Research Institute, the University of Tokyo.
5-1-5 Kashiwanoha, Kashiwa, Chiba 277-8568, Japan
E-mail: hiro@aori.u-tokyo.ac.jp

ABSTRACT

To obtain physical insights into the response and feedback of low clouds (C_l) to global warming, ensemble 4×CO_2 experiments were carried out with two climate models, the Model for Interdisciplinary Research on Climate (MIROC) versions 3.2 and 5. For quadrupling CO_2, tropical-mean C_l decreases, and hence, acts as positive feedback in MIROC3, whereas it increases and serves as negative feedback in MIROC5.

Three time scales of tropical-mean C_l change were identified—an initial adjustment without change in the global-mean surface air temperature, a slow response emerging after 10-20 years, and a fast response in between. The two models share common features for the former two changes in which C_l decreases. The slow response reflects the variability of C_l associated with the El Niño-Southern Oscillation in the control integration, and may therefore be constrained by observations. However, the fast response is opposite in the two models and dominates the total response of C_l. Its sign is determined by a subtle residual of the C_l increase and decrease over the ascending and subsidence regions, respectively. The regional C_l increase (decrease) is consistent with a more (slightly less) frequent occurrence of a favourable condition for C_l, as measured by lower-tropospheric stability (LTS), over the aoscending (subsidence) region. The above frequency change in LTS is similarly found in six other climate models despite a large difference in both the mean and the changes in the low-cloud fraction for a given LTS. This suggests that the response of the thermodynaomic constraint for C_l to increasing CO_2 concentrations is a robust part of the climate change.

Keywords: low clouds, climate model, lower-tropospheric stability, 4×CO_2

1. Introduction

The global climate model (GCM) is a unique tool for simulating Earth's climate in a physically-based manner. GCMs have been improved for the past decades (Reichler and Kim 2008) and extensively used in the Intergovernmental Panel on Climate Change (IPCC) Assessment Reports (Solomon et al. 2007). While many aspects of the climate simulated in GCMs, such as temperature and wind fields, are much more realistic than in the past, the representation of clouds remains one of their largest limitations. Indeed, the current IPCC-class models show a substantial divergence in terms of sign and magnitude of the cloud-radiative feedback in response to increase in atmospheric CO_2 concentration (e.g, Bony and Dufresne 2005; Soden and Held 2006; Webb et al. 2006). In particular, shortwave radiative feedbacks associated with changes in low clouds (combination of stratiform, stratocumulus, and shallow cumulus clouds) remain largely unknown; they act as negative feedback in some GCMs, but vice versa in the others.

It is widely recognized that the tropical low-level cloud fraction (C_l), a major player in the global cloud shortwave forcing, is partly controlled by the large-scale environment, especially over the subsidence regime. Klein and Hartmann (1993), and later Wood and Bretherton (2006), revealed that the inversion strength above the planetary boundary layer (PBL) provides a good measure of the distribution and seasonal cycle of C_l. This thermodynamic constraint is typically measured in terms of lower-tropospheric stability (LTS), defined by the difference in potential temperature (θ) between the 700 and 1000 hPa levels. There is also a dynamic constraint that affects C_l as measured by the vertical pressure velocity at 500 hPa (ω_{500}) or the low-level divergence (Zhang *et al.* 2009). Several studies have shown that the cloud properties sorted using these quantities reveal well the distinct cloud regimes in the GCMs (Wyant et al. 2006; Su et al. 2008; Medeiros and Stevens 2011).

In reality, the physics of low clouds are complex phenomenon involving mutual interaction between the large-scale environment and the local processes of turbulence, cloud microphysics, convection, and radiation. Therefore, it is difficult to construct a simple theory of low-cloud physics and their response to climate change. Yet, several works have proposed a simplified model for low clouds (Miller 1997; Larson et al. 1999; Caldwell and Bretherton 2009). They argue a possible negative low-cloud feedback in a warmed climate. When there is non-uniform change in sea surface temperature (SST) in the tropics, this negative feedback results from thinning of the PBL, increased LTS, and thickened cloud layer. These changes are not fully investigated in the climate change simulation by GCMs.

There have been attempts to estimate climate sensitivity and cloud radiative feedback based solely on observations, which, if possible, greatly reduce the uncertainty in climate change projections. However, these observational estimates still suffer from large errors due to the short periods covered by the data as well as the uncertainty in the measurements (Forster and Gregory 2006; Murphy et al. 2009). A more critical question is whether the climate feedback estimated for the natural variability that dominates the short record is applicable to the feedback in long-term climate change due to radiative forcing. Clement et al. (2009) discussed low-cloud feedback associated with the Pacific decadal oscillation, by combining satellite cloud products and GCM simulations. They concluded that the low clouds over the northeastern Pacific serve as a positive feedback, and further suggested a similar feedback at work over the entire Pacific under global warming. Such an extrapolation may, however, be controversial since the metric constructed over a particular regime is used for arguing the cloud feedback in other regimes. Dessler (2010) identified a positive cloud shortwave feedback in short-term variations in satellite and reanalysis data and also in climate models, but found that they are not correlated with the cloud feedback in response to long-term climate change. Thus, cloud feedback is apparently dependent on the time scale, which is the major focus of the present study.

Gregory and Webb (2008) demonstrated that, in GCMs, clouds can change without any change in the global-mean surface air temperature (SAT). This occurs rapidly as part of the tropospheric adjustment due directly to the radiative forcing caused by increased CO_2 levels. In contrast to this rapid adjustment, cloud changes in response to changing SAT are often called 'slow feedback'. However, the above observational studies and a recent GCM study by Held et al. (2010) suggest that cloud feedback can also be classified according to the time scales. In the present study, the cause and timescale-dependence of tropical low-cloud feedback are examined using two GCMs, the Model for Interdisciplinary Research on Climate (MIROC) versions 3.2 and 5, which show an opposite sign of the cloud shortwave feedback to climate change (Watanabe et al. 2010). We intend to examine the extent to which the C_l change can be constrained by properties of the model's natural variability, but not to conclude which version gives the correct C_l change. Furthermore, a robust part of the environmental changes related to C_l, which will be identified by comparing the two models, is verified by analysing outputs from six other GCMs.

The present paper is organized as follows. In Sect. 2, two versions of MIROC and abrupt 4×CO_2 experiments are described. Several observational data sets for validating the simulated cloud fields are also explained. In Sect. 3, the natural low-cloud variability and its mechanism are examined using the model control runs and observations. The results are then applied in Sect. 4 to understand the low-cloud response to changes in radiative forcing. In particular, we emphasize the multiple time scales of the response, in which the property of the natural low-cloud variability plays a partial role. In Sect. 5, the analysis is extended to the multi-model outputs obtained from the Coupled Model Intercomparison Project phase 3 (CMIP3), in order to identify a robust portion of the low-cloud response. Section 6 presents the concluding discussion.

2. Model and experiments

a. MIROC3.2

MIROC version 3.2 (denoted as MIROC3.2) is a full atmosphere-ocean-land-sea ice coupled model, jointly developed at the Center for Climate System Research (CCSR)[1], the University of Tokyo, National Institute for Environmental Studies (NIES), and the Japan Agency for Marine-Earth Science and Technology (JAMSTEC) (K-1 model developers 2004). This version of MIROC contributed to the IPCC Fourth Assessment Report (AR4). The atmospheric component model, including a multi-layer land model, employs a spectral dynamical core and implements a standard physics package which also incorporates a simplified aerosols module. The ocean and sea-ice models comprise the CCSR ocean component model (COCO). The resolution of the atmospheric model is T42L20 and the ocean component has approximately 1° grid spacing. They correspond to the 'MIROC3.2med' abbreviated in the IPCC AR4.

b. MIROC5

[1] Renamed the Atmosphere and Ocean Research Institute as of April, 2011.

We have upgraded MIROC3.2 to the latest version 5.0, denoted as MIROC5, which will be used for the IPCC Fifth Assessment Report (AR5). The basic framework of MIROC5 follows that of MIROC3.2, but many of the parameterization schemes in the atmospheric model have been replaced either by implementing recent ones or by schemes newly developed by our group. In particular, it is important to state for the present study that the following significant changes were made in the treatment of turbulence and clouds in MIROC5: the level 2.5 turbulence closure, prognostic cloud scheme, cloud microphysics, and a prognostic scheme for number concentrations of cloud droplets and ice crystals (see Watanabe et al. 2010 for details). The ocean and sea-ice fields are also calculated with an updated COCO. The standard resolution of the atmospheric model is T85L40, which is double that of MIROC3.2, while the ocean component employs almost the same horizontal resolution as that used in MIROC3.2. We conducted a 500-yr pre-industrial control simulation, which shows improvements in both the mean state and natural climate variability (Watanabe et al. 2010). For example, the features of the El Niño-Southern Oscillation (ENSO) are more realistic in MIROC5. Furthermore, the importance of a new cumulus convection scheme in the ENSO simulation was identified through perturbed parameter experiments (Watanabe et al. 2011a).

c. 4×CO_2 experiments

The pre-industrial control experiments are first carried out with atmospheric CO_2 concentration of 285 ppm. We then take the initial conditions from the control runs, which are at least 20 yrs apart to avoid overlapping of the 4×CO_2 experiments. From each of the initial states, the models are integrated for 20 yrs with an abrupt quadrupling of the CO_2 concentration from 285 to 1140 ppm. This concentration does not mimic the possible level of CO_2 in climate change scenarios but rather sets to increase the signal-to-noise ratio, as recommended in CMIP5 (cf. experiments 6.3 and 6.3E). A ten- and six-member ensemble is made with MIROC3.2 and MIROC5, respectively. The period of integration is short for the model's climate to be equilibrated, but long enough to estimate the effective climate sensitivity (Gregory et al. 2004). However, these ensembles do not represent a slowly evolving response of the climate system; therefore, we extended one member up to 150 yrs. The response of the variable x to the radiative forcing due to the quadrupled CO_2 concentration is evaluated using annual-mean fields and is denoted as Δx. We recognize the uncertainty associated with clouds due to interaction of clouds with both the radiation and meteorological fields, but focus in this study on the latter without arguing the cloud-radiative processes.

d. CFMIP1 database

A systematic comparison of clouds simulated in GCMs has been proposed in the Cloud Feedback Model Intercomparison Project phase 1 (CFMIP1; http://cfmip.metoffice.com), which collected a dataset of equilibrium control and $2\times CO_2$ experiments using coupled atmosphere-slab ocean models. The CFMIP1 data have so far been extensively used to analyse the cloud regime in control experiments as well as to examine cloud feedback in climate change simulation (Webb et al. 2006; Williams et al. 2006; Ringer et al. 2006; Tsushima et al. 2006; Williams and Tselioudis 2007). We use the CFMIP1 data in this study and compare them with the cloud response identified in our two models; note that data from MIROC3.2 has also been submitted to CFMIP1. The data used are obtained from six models: the Canadian Centre for Climate Modelling and Analysis (CCCma) low-resolution version, National Center for Atmospheric Research (NCAR) CCSM3, Geophysical Fluid Dynamics Laboratory (GFDL) CM2.0, Goddard Institute for Space Studies (GISS) ER, Institute for Numerical Mathematics (INM) CM3.0, and the Meteorological Research Institute (MRI) CGCM2.3.2. Each model provides a single member integrated for 20 yrs, from which we define Δx as in the MIROC outputs.

e. Observational data

To validate the cloud fields in the control experiments, we use two satellite-based low-cloud datasets. One is obtained from the International Satellite Cloud Climatology Project (ISCCP) (Rossow and Schiffer 1999). The ISCCP provides the longest term satellite cloud data, for 1984-2007 on a regular 2.5º grid. The other is derived from the Cloud-Aerosol Lidar and Infrared Pathfinder Satellite Observation (CALIPSO) (Winker et al. 2009). The CALIPSO data are limited for the recent few years from January 2006 to November 2008, but are able to capture a fine horizontal structure of clouds.

In addition to the satellite-derived cloud data, we use observations of SST for 1945-2006 derived from Ishii et al. (2006) and of the atmospheric fields obtained from two reanalyses: the Japanese 25-yr reanalysis (JRA25) (Onogi et al. 2007) for 1979-2009 and the European Centre for Medium Range Weather Forecasts (ECMWF) 40-yr reanalysis (ERA40) (Uppala et al. 2005) for 1979-2001. These are all monthly basis and analysed in order to identify environmental conditions associated with past low-cloud variability.

For the cloud regime analysis performed in Sect. 5, we newly compiled the cloud data using CloudSat and CALIPSO and the cloud mask scheme C4, ‘CloudSat or

CALIPSO' scheme, in which clouds are detected by at least one of these two satellites (Hagihara et al. 2010). The scheme was developed on the basis of cloud masks derived from shipborne 95GHz cloud radar and lidar observations in the western Pacific Ocean near Japan and in the tropical western Pacific (Okamoto et al. 2010, references therein). Radar reflectivity was derived from the CloudSat 2B GEOPROF product (release R04), in which a confidence level value ≥20 was applied to determine cloudy pixels from CloudSat (Marchand et al. 2008). The minimum detectable signal radar reflectivity is about -30 dBZ, implying that some cloud regions were not detected. This underestimation of cloud detection may account for more than 10% of low-level clouds, based on ship-based radar measurement. CALIPSO lidar level 1B (version 2.01) products were used as lidar backscattering coefficients for co- and cross-polarization at 532 nm wave length. The CALIPSO cloud mask C2 used in this study is different from the standard cloud mask, vertical feature mask (VFM) (http://eosweb.larc.nasa.gov/PRODOCS/calipso/Quality_Summaries/). We first applied a threshold of the total backscattering coefficient at 532 nm to the target grid. The threshold depended on the background noise signal (estimated at 19–20 km altitude), the molecular signal derived from the ECMWF data. Next, the spatial continuity was tested using the surrounding 5 × 5 bins at altitudes < 5 km, and 9 × 9 bins at altitudes > 5 km. The cloud mask results were then averaged to obtain the same vertical and horizontal resolutions as the CloudSat data (1.1 km and 240 m). It is worth noting that the cloud mask results for CALIPSO have less contamination by noise and aerosols at low altitude levels compared with the CALIPSO standard VFM (Hagihara et al. 2010; Okamoto et al. 2010).

3. Natural low-cloud variability

As a prelude to the low-cloud response to increasing CO_2 in GCMs, the property of natural low-cloud variability is compared between the observations and the models. The definition of low cloud (hereafter denoted as C_l) follows ISCCP (Rossow and Schiffer 1999). As stated in the introduction, the formation and dissipation of stratocumulus and shallow cumulus clouds, the major components in C_l, are partly controlled by large-scale environmental factors such as vertical motion and inversion strength. We therefore compare the local correlation between the monthly C_l anomalies and the anomalies of either ω_{500} or LTS. The ω_{500} field represents a dynamic constraint whereas LTS provides a thermodynamic constraint on C_l.

The observed correlation maps for 1984-2007 based on ISCCP and JRA reanalysis reveal that the C_l anomaly is overall positively correlated with both ω_{500} and LTS (Fig. 1a,b). In particular, the C_l variability is strongly coupled with the in-situ ω_{500} (LTS) over the equatorial (subtropical) regions where the mean SST is higher (lower) than roughly 26 °C. While the influence of ω_{500} and LTS to C_l is generally complementary in terms of the geographical distribution, both factors affect C_l in some regions such as the subtropical western Pacific and the southern Indian Ocean.

Correlation maps for the 150-yr control runs using MIROC3.2 and MIROC5 are shown in the remaining panels of Fig. 1. The C_l-ω_{500} and C_l-LTS relationships show several discrepancies compared to the observations: weak dynamical coupling over the tropical western Pacific and stronger thermodynamic coupling near the equator in MIROC3.2 (Fig. 1c,d), and a banded structure in the C_l-LTS relationship in MIROC5 (Fig. 1f). Yet, the broad features of the dynamic and thermodynamic coupling with C_l appear to be reproduced in the two models.

Given the strong local coupling of C_l with ω_{500} and LTS, which are ultimately maintained by the underlying SST, we attempt to extract the leading mode of variability in the natural C_l variability together with the dominant pattern of the SST variability. For this purpose, singular value decomposition (SVD) analysis is applied to the monthly C_l and SST anomalies over the tropical oceans between 30º S and 30º N. To obtain robust observational estimates, two sets of cloud and SST data are used: monthly SST by Ishii et al. (2006) and ISCCP cloud products[2] from July 1983 to June 2005 (Fig. 2a,b), and NOAA OISST and CALIPSO data from June 2006 to November 2008 (Fig. 2c,d). Despite the different sources and periods of data, both sets show the leading SVD very similar to each other; the SST anomaly pattern clearly represents the ENSO warm phase and the associated C_l fields show the reduction over the positive SST anomaly and vice versa. Because the SST and C_l anomalies are not uniform in space, the tropical-mean C_l anomaly associated with the leading SVD is small but slightly negative.

Figure 2a-d suggests that the dominant C_l variability in the tropics is the response to ENSO, so that the reproducibility in the GCMs may depend on the ability of the ENSO simulation. It has been reported that MIROC5 produces a more realistic ENSO in terms of the spatial structure and amplitude (Watanabe et al. 2010). This, in fact, is seen in the difference in the leading SVD patterns (Fig. 2e-h). The SST anomaly pattern in MIROC3.2 lacks the horse-shoe shaped cooling in the western Pacific and thereby the uniform negative anomaly dominates the C_l field (Fig. 2e-f). The anomaly patterns in MIROC5 have more resemblance to the observational counterparts (Fig. 2g,h).

The leading SVDs, possibly representing ENSO and its driving of C_l, account for

[2] As discussed in Clement et al. (2009), some C_l signals might be included in the mid-level cloud data in ISCCP. We tested the analysis to both low-cloud data and merged low- and mid-cloud data separately, but the results were not significantly different. Therefore, we present only the SVD based on the original low-cloud data.

40-70% of the total covariance; this suggests that a measure for ENSO can be used to explain the tropical-mean C_l anomaly. This idea is tested by plotting the area-weighted, tropical-mean C_l anomaly (30º S and 30º N over oceans, denoted as $\langle C_l' \rangle$) against the Niño 3 SST anomaly (Fig. 3a-c). The tropical average is affected by regional errors and a bias in the ISCCP C_l field, so we used the monthly $\langle C_l' \rangle$ time series from January 2006 to November 2008 based on the CALIPSO data. It shows a negative correlation with the Niño 3 SST anomaly (r = -0.47) and reveals a 0.44% decrease per 1K increase in SST (Fig. 3a). A similar negative correlation is found in the two GCMs, but the regression slope in MIROC3.2 is larger and indicative of higher sensitivity of $\langle C_l' \rangle$ to ENSO (Fig. 3b,c).

The C_l response to ENSO will be partly generated via changes in the large-scale environment. By referring to ω_{500} as an environmental variable, the C_l anomaly, C_l', is expressed following Bony et al. (2004):

$$\tilde{C}_l' \simeq \int_\omega P_\omega' \bar{C}_l(\omega) d\omega + \int_\omega \bar{P}_\omega C_l'(\omega) d\omega \quad , \tag{1}$$

where $\tilde{C}_l'$ denotes the reconstruction of C_l', $\bar{P}_\omega$ and P_ω' are the probability density functions (PDFs) of the ω_{500} climatology and anomaly, respectively, and $\bar{C}_l(\omega)$ and $C_l'(\omega)$ are the climatology and anomaly of the composite C_l with respect to ω_{500}. The first term is often called the dynamic component whereas the second term is known as the thermodynamic component of the cloud regime. When (1) is applied to the ENSO-related anomalies, $\langle C_l' \rangle$ is well reproduced both in observations and models (root mean square errors are 0.27, 0.12, and 0.39% for Fig. 3a-c). The contribution of each component can then be seen in the scatterplot of the two terms in (1) against $\langle \tilde{C}_l' \rangle$, which shows that the observed $\langle C_l' \rangle$ variability mostly occurs thermodynamically, i.e., without change in P_ω (Fig. 3d). This thermodynamic driving of $\langle C_l' \rangle$ is qualitatively reproduced in MIROC5, but not in MIROC3.2 (Fig. 3e,f).

To summarize, the above results indicate that the tropical-mean C_l variability in the absence of any change in radiative forcing, i.e., the natural variability, is governed by ENSO and occurs through thermodynamic processes. These observed features are better reproduced in MIROC5. However, it may not guarantee that the response of C_l to the change in radiative forcing in MIROC5 is more reliable than that in MIROC3.2. The question of how the natural variability is related to the externally induced climate change is examined in the next section using the 4×CO_2 experiments.

4. Three timescales of the low-cloud response

a. Adjustment, fast and slow responses

Following previous studies that showed a quasi-linear relationship between the changes in the global-mean radiative budgets and in SAT under the doubling of CO_2 (Gregory et al. 2004; Gregory and Webb 2008), we use the global-mean SAT response, denoted as $\Delta\mathrm{SAT_g}$, defined by the annual- and ensemble-mean difference between the control and 4×CO_2 experiments for each model. Assuming that the radiatively forced response of x, i.e., Δx, can be represented by a linear function of $\Delta\mathrm{SAT_g}$, we write

$$\Delta x \approx \alpha_x \Delta\mathrm{SAT}_g + \Delta x_0 \qquad (2)$$

where α_x is the regression slope of Δx against $\Delta\mathrm{SAT_g}$ while Δx_0 is the interception. By definition, Δx_0 represents a component of Δx occurring without change in $\mathrm{SAT_g}$ and hence is referred to as the ‘adjustment’. The rate of response proportional to $\Delta\mathrm{SAT_g}$, α_x, measures the sensitivity of x to the global-mean surface warming and is called 'feedback' throughout the paper. Specifically, a change in x may not necessarily feedback to SAT, but we use the term (except for α_{SAT}) in an analogical sense to the change in radiative fluxes. Both the adjustment and feedback are evaluated on an annual basis using 20-yr ensemble runs, so that the number of samples becomes 200 and 120 for MIROC3.2 and MIROC5, respectively.

The local α_{SAT} is first presented in Fig. 4a,c. The surface warming patterns are similar to each other in several aspects: larger warming over land than over the ocean, well-known polar amplification around the Arctic, and less warming or slight cooling over the Antarctic circumpolar region. These features have been identified in realistic climate change simulations (Solomon et al. 2007). Given the fact that the change in global-mean radiative fluxes either at the top of atmosphere or on the surface is well fitted by (2), and that the change in cloud shortwave radiation is greatly affected by the change in low cloud (Klein and Hartmann 1993), we would expect a quasi-linear relationship between the global-mean ΔC_l and ΔSAT_g, which is, however, not observed (Fig. 4b,d). For the first 20 yrs, the ensemble- and global-mean ΔC_l tends to show a monotonic decrease in MIROC3.2 and increase in MIROC5 (blue symbols). Afterwards, ΔC_l appears to fluctuate more independently of ΔSAT_g, as indicated by the weak correlation of r = -0.21 and -0.23.

We calculated the correlation of the local ΔSAT and the global-mean ΔC_l using the 150-yr single run, which revealed that the global-mean ΔC_l is highly correlated with ΔSAT over the eastern equatorial Pacific (not shown). This suggests that the global-mean ΔC_l is better explained in terms of the projection on to the natural variability shown in Fig. 2. Because of a great similarity in the temporal evolution between the global-mean and tropical-mean ΔC_l, we use ΔC_l averaged over the tropical oceans (30º S - 30º N) and plot it against ΔSST in the Niño 3 region (Fig. 5). It is evident that ΔC_l is more coherent with the Niño 3 ΔSST than ΔSAT_g; the correlation after 20 yrs reaches r = -0.86 and -0.69 in MIROC3.2 and MIROC5, respectively. It is interesting to note that the regression slope, -0.59 and -0.25% K^{-1}, is nearly identical to the slope obtained from the natural variability presented in Fig. 3b,c (also represented by the dashed lines in Fig. 5). This coincidence implies that ΔC_l on a time scale longer than 20 yrs can be constrained by the natural variability associated with ENSO, which has observational counterparts. By referring to Fig. 3a as the observational estimate, the slow negative C_l feedback may be overestimated in MIROC3.2. Since the annual-mean changes in a single run include natural variability, one may suspect that the slope of the slow change simply reflects the internal fluctuation in a quasi-equilibrated climate but not the forced response. It is, however, not true, and the decadal-mean changes (red circles in Fig. 5) indeed show the decreasing/increasing tendency well fitted by the slope of the internal variability.

While it is encouraging that a part of ΔC_l can be constrained by natural variability, Fig. 5 reveals that the total ΔC_l averaged over the entire period is not determined by the slow response. During the first few years, ΔC_l tends to be negative in MIROC3.2 while positive in MIROC5, as seen in the ensemble-mean response for the 20-yr runs (blue symbols in Fig. 5). It is this fast response that determines the sign of the low-cloud response in the two models. The mechanism of the fast response is therefore the heart of the low-cloud change to $4\times CO_2$ as will be elaborated in Sect. 4b.

It is clear that ΔC_l depends on ΔSST in a nonlinear fashion, hence Δx_0 in (2) may not be a good measure for the initial adjustment of clouds. We therefore used ΔC_l at the initial month of the ensemble, as presented by stars, which show a slight reduction of -0.23 and -0.28% in MIROC3.2 and MIROC5. This decrease is almost independent of both ΔSAT_g and the Niño 3 ΔSST, and is discussed further in this section.

In simple models for low clouds, the change in C_l is often argued to be coupled with changes in the PBL thickness, Z_{PBL} (Larson et al. 1999; Caldwell and Bretherton 2009). The adjustment component of Z_{PBL} is shown in Fig. 6a,b. Because of the different turbulence scheme, the mean Z_{PBL} is somewhat different between MIROC3.2 and MIROC5, the latter showing deeper PBL (contours in Fig. 6a,b). Nevertheless, the patterns of ΔZ_{PBL0} appear to be similar to each other in terms of sign and magnitude; they both show the initial shoaling of the PBL. Interestingly, the 'feedback' component of Z_{PBL} is much smaller (not shown), indicating that Z_{PBL} is sensitive to the direct radiative forcing but not so to slow SST increases.

Among the various factors controlling Z_{PBL}, such as buoyancy flux at the surface, cumulus mass flux, and LTS, the buoyancy input from the surface plays a dominant role over the tropical oceans (Medeiros et al. 2005). Indeed, the adjustment components of the surface heat flux (sum of the sensible and latent fluxes, denoted as Q) are negative over most of the tropical oceans (Fig. 6c,d). They indicate the reduction of buoyancy production required for deepening the PBL and thereby seem to explain the negative ΔZ_{PBL0}. In the tropospheric adjustment process, Q is known to change without any change in SAT_g (Gregory and Webb 2008). Andrews et al. (2009) demonstrated that the positive downward radiative forcing is smaller at the surface than at the tropopause, which results in a rapid reduction in Q to accomplish the energy balance in the troposphere (cf. their Fig. 8). The results shown in Fig. 6c,d are consistent with this argument and a thinner PBL and low-cloud layer are thus a robust part of the tropospheric adjustment at least in the two models.

b. Mechanism for fast response

We need to elucidate the reasons why the tropical-mean ΔC_l decreases in MIROC3.2 and increases in MIROC5 on a fast time scale (Fig. 4b,d). For this purpose, the 'feedback' components, α in (2), are calculated for C_l , ω_{500}, LTS, and SST using the ensemble of 20-yr runs. It should be noted that a positive C_l feedback means an increase of C_l in response to the positive ΔSAT_g, corresponding to a negative cloud shortwave feedback.

Figure 7a,b compares the feedback for C_l over the tropical oceans in MIROC3.2 and MIROC5. As SAT_g increases, C_l decreases over the equatorial Pacific while increasing over the southern subtropics in both models. A major difference is found over the Indian Ocean and the northern subtropical Pacific, where C_l decreases in MIROC3.2 but increases in MIROC5. The C_l feedback patterns are consistent with feedbacks in both ω_{500} and LTS (Fig. 7c-f). The ω_{500} feedback, $\alpha_{\omega,}$ is negative over the equatorial Pacific and positive over the mean ascending regions, indicating a slowdown of the tropical circulation. This response is similarly found in the two models as well as being reported in realistic scenario experiments (e.g., Vecchi et al. 2006). The LTS feedback, α_{LTS}, is overall positive in the tropics, but shows a horizontal inhomogeneity in its magnitude; α_{LTS} is relatively small (large) over the equatorial (southern subtropical) Pacific where the C_l feedback is negative (positive). Over the western off-equatorial Pacific, both α_ω and α_{LTS} are large in MIROC5 compared to MIROC3.2, which appears to match the greater increase in C_l (Fig. 7b,d,f).

The fast response of the atmosphere occurring over several years can ultimately be attributed to changes in the tropical SST that responds to the radiative forcing even on such a time scale. Figure 7g,h shows that SST warms as much as SAT_g during the 20-yr period, i.e., $\alpha_{SST} \sim 1$. Yet, the warming is not uniform and a greater SST increase accompanies a smaller increase in LTS and an ascending tendency in ω_{500}, for example, over the central-eastern equatorial Pacific in MIROC5. This correspondence of the spatial patterns between changes in SST, LTS, ω_{500} and C_l has been identified in realistic climate change simulations as well (Watanabe et al. 2011b). Despite the warming of the ocean surface everywhere in the tropics, α_{LTS} is positive, which indicates more warming of the lower troposphere above the PBL. The entirely positive α_{LTS} is in contrast to the pattern of α_ω, which cannot be uniformly positive or negative in accordance with the mass conservation of the tropical air mass. This suggests that the tropical-mean, but not regional C_l response is primarily controlled by the change in stability but not the circulation.

In order to verify the above inference, the cloud regime composite used in Sect. 3 is applied to the fast response. Namely, (1) is rewritten for Δ:

$$\Delta\tilde{C}_l \simeq \int_\omega \Delta P_\omega C_l^{\mathrm{CTL}}(\omega)d\omega + \int_\omega P_\omega^{\mathrm{CTL}} \Delta C_l(\omega)d\omega \qquad (3a)$$
$$\simeq \int_s \Delta P_s C_l^{\mathrm{CTL}}(s)ds + \int_s P_s^{\mathrm{CTL}} \Delta C_l(s)ds \qquad (3b)$$

where $\Delta\tilde{C}_l$ is the reconstruction of ΔC_l, P_ω^{CTL} the mean PDF in the control run, ΔP_ω the PDF difference between the control and the 4×CO_2 runs, $C_l^{\mathrm{CTL}}(\omega)$ and $\Delta C_l(\omega)$ are similar to P_ω^{CTL} and ΔP_ω but for the composite of C_l with respect to ω_{500}. The subscript of ω in (3a) can be replaced with LTS, denoted as s in (3b). When we choose ω_{500} as a reference, the first (second) term represents the dynamical (thermodynamic) component of $\Delta\tilde{C}_l$ and vice versa for s. It is possible to construct a joint PDF using ω_{500} and s, but we carried out the calculation separately because the two variables are not independent (not shown). The regime composite of the observed C_l anomaly on the two-dimensional phase plane has been computed by Medeiros and Stevens (2011), who show that the C_l anomaly depends more on s (cf. their Fig. 2).

The regime composite $C_l^{\mathrm{CTL}}(\omega)$, and P_ω^{CTL} are represented by blue curves in Fig. 8a,c. As is well known, most of the tropics are occupied by weak subsidence except for a small area having a strong ascent; P_ω^{CTL} is thus skewed in both models. When $C_l^{\mathrm{CTL}}(\omega)$ is compared with satellite observations (cf. Fig. 1 of Bony and Dufresne 2005), MIROC3.2 (MIROC5) is found to underestimate (overestimate) the amount of C_l in the subsidence (ascent) regime. Nevertheless, the C_l responses, i.e. $\Delta C_l(\omega)$, in each regime resemble each other: increasing for $\omega_{500} < 0$ and decreasing for $\omega_{500} > 0$. This indicates that, in spite of the opposite sign of the tropical-mean ΔC_l, low cloud is suppressed in the 4×CO_2 runs over the subtropical cool oceans where $C_l^{\mathrm{CTL}}(\omega)$ dominates. The tropical-mean ΔC_l is determined by a subtle residual; the $C_l(\omega)$ reduction in the subsidence regime is prevailing over the enhancement in the ascent regime, leading to the net decrease in MIROC3.2, and vice versa in MIROC5. A certain difference between $C_l^{\mathrm{CTL}}(\omega)$ and $C_l^{\mathrm{CTL}}(\omega) + \Delta C_l(\omega)$, together with a similarity between P_ω^{CTL} and $P_\omega^{\mathrm{CTL}} + \Delta P_\omega$, clearly indicates that the thermodynamic change in each cloud regime is the major factor for $\Delta\tilde{C}_l$.

The thermodynamic constraint to ΔC_l is expressed in terms of the PDF for LTS, ΔP_s, in (3b). Indeed, $P_s^{CTL} + \Delta P_s$ is displaced toward a higher value in both models, resulting in a positive contribution to $\Delta\tilde{C}_l$ (Fig. 8b,d). The composite of $\Delta C_l(s)$ is negative for large LTS, indicating that the second term in (3b) works to reduce C_l. The shift in P_s is small in MIROC3.2. Because of this and underrepresentation of the mean $C_l(s)$, the thermodynamic contribution $\Delta P_s C_l^{\mathrm{CTL}}(s)$ will be small and thus cannot overcome the negative effect due to the dynamic component in MIROC3.2. To summarize, both similarities and differences are identified in the cloud regime changes in the two models. The major similarity is the dominant thermodynamic driving of ΔC_l in which a more stable condition, as represented by ΔP_s, should favour a positive ΔC_l. The differences are mostly in the quantitative sense, e.g., smaller ΔP_s in MIROC3.2 which, however, determines the sign of the tropical-mean ΔC_l. In order to examine the extent to which the similarity found between the two models is generally valid, we analyse the multi-model outputs obtained from the CFMIP1 in the next section.

5. Robust thermodynamic changes in CFMIP models

Given the dominant thermodynamic effect on ΔC_l in MIROC, we extend the regime analysis to outputs from the CFMIP1 models. We use cloud fraction but not C_l because the models providing temperature and/or ω_{500} lack the C_l data obtained from the ISCCP simulator. The composite cloud fraction sorted by LTS is calculated either on the model level or on the pressure level and then collectively plotted in Fig. 9. For reference, we computed a similar composite diagram using the CALIPSO data (see Sect. 2e for the method).

Before examining the cloud changes in 2×CO_2 and their differences among the models, we compare the mean cloud fraction between CALIPSO and GCMs (shading in

Fig. 9). The satellite-based estimate of the cloud fraction (Fig. 9a) reveals the following characteristics: a maximum of more than 30% occurring at the highest value of LTS, and a gradual increase of the cloud layer altitude as LTS decreases. These features of the mean low cloud fraction may also be seen when we make the longitude-height section along the subtropical eastern oceans (Wang et al. 2004). All the GCMs not only fail to reproduce the cloud distribution derived from CALIPSO but also show different types of bias. Namely, low clouds are overestimated for low LTS in MIROC5, CCSM3, and GISS ER, whereas overall they are underestimated in MIROC3, CCCma, and GFDL CM2.0. The cloud layer is too thin in MRI GCM. The causes of these biases would involve various factors and are beyond the scope of this study, but we need to bear them in mind when comparing the cloud change in the 2×CO_2 runs.

The divergence of the mean cloud distribution in GCMs prevents us from detecting and understanding the consistent change in the cloud fraction in the 2×CO_2 experiments (contours in Fig. 9). Yet, we can identify some consistency although it may not necessarily explain the different magnitude and sign of the total low-cloud change. For example, a relatively large change in the cloud fraction is found at small LTS in models that overestimate the mean cloud there (e.g., MIROC5, CCSM3, and GISS ER). At large LTS, many models show an increase and decrease of clouds above and below the mean cloud layer, suggesting an upward shift of the cloud layer. This accompanies an asymmetry in the cloud amount change, either a greater increase (e.g., MIROC5, CCSM3, and GISS ER) or decrease (e.g., MIROC3, INM, and MRI), probably resulting in a non-zero change of the low-cloud amount.

Despite large differences in the mean cloud fraction and its changes among GCMs, the change in the thermodynamic condition P_s has a common structure, which represents a shift of the PDF peak to larger values (bottom panels in Fig. 9). While the degree of the PDF shift depends on the model (for example, it is large in CCSM3 but small in INM), this coincidence indicates that the changing thermodynamic constraint as found in the two MIROC models (Fig. 8b,d) is a robust part of the climate change. If the cloud change at a given LTS (contours) does not prevail, this thermodynamic effect should act to increase the low cloud in all the models.

The positive shift of P_s, i.e. increased stability, can also be represented on a geographical map by defining the frequency of the stable condition:

$$f_s = \frac{1}{N}\sum_n \delta_n \quad , \ \delta_n = \begin{cases} 1 & \text{for } s_n \geq s_0 \\ 0 & \text{otherwise} \end{cases} \tag{4}$$

where N indicates the number of samples at a grid point (N = 240), and s_0 is the threshold of the LTS. In the reanalysis, we may set s_0 = 15 K (shaded region in Fig. 9a). For the GCMs, we need to take the mean bias into account, so that the value is defined for each model: s_0 = 15 K for CCCma, INM CM3.0, and MRI CGCM2.3.2, s_0 = 16 K for NCAR CCSM3, and s_0 = 13 K for GFDL CM2.0, GISS ER, and MIROC. The choice of s_0 is somewhat subjective, but the area of f_s greater than 0.9 in the control runs (contours in Fig. 10) indicates that it is indeed capturing the mean subtropical low-cloud regions in all the models.

As expected, the change in f_s to the radiative forcing, i.e Δf_s, is overall positive in the tropics, and shows similar spatial patterns among the models. Remarkably, a weak positive Δf_s is commonly found over the subtropical Pacific and Atlantic. In contrast to the diversity in magnitude and sign of Δf_s near the equator, this robust response in the subtropics suggests that the shallow trade cumulus clouds are stimulated by the frequent occurrence of stable conditions. It is somewhat surprising that Δf_s is small or even negative over the eastern subtropical oceans where the mean f_s is large. These areas mostly satisfy a condition of high LTS in the control runs, which may therefore not change drastically under the warmed climate.

6. Concluding discussion

Motivated by the fact that the two different versions of the climate model MIROC show opposite signs of cloud shortwave feedback to global warming (positive feedback in MIROC3.2 and negative feedback in MIROC5), we investigated the mechanisms of the tropical low-cloud response to abrupt increases in atmospheric CO_2 concentration using two sets of ensemble $4\times CO_2$ experiments based on those models. The major results are summarized as follows.

1) An initial reduction in the tropical-mean C_l occurs in both models, which is likely the result of the positive cloud shortwave forcing (Fig. 18 of Watanabe et al. 2010). The decrease of C_l is accompanied by a shoaling of the PBL due to suppressed surface heat fluxes (Fig. 6), possibly as a part of the tropospheric adjustment.

2) The feedback of C_l can be separated into two timescales: fast and slow components, emerging during the first several years and after about 20 yrs, respectively. The slow component commonly shows a gradual decrease of the tropical-mean C_l, the rate of which matches well with the slope determined by the C_l response to ENSO in the control runs.

3) The fast component in the two models shows an opposite sense of decrease in MIROC3.2 and increase in MIROC5, which are crucial for the total C_l response and consistent with the different cloud shortwave feedbacks between the two models. However, changes in the C_l regime diagram, i.e. the decrease over the subsidence

regime and increase over the other subtropical regions where a thermodynamic condition favourable for C_l happens more frequently, are qualitatively similar to each other. The sign of the tropical-mean C_l is thus determined by a subtle residual of the increase and decrease of the regional C_l.

4) The frequency change in the thermodynamic condition measured by LTS is similarly found in six other climate models despite a large difference of both the mean and the changes in the low-cloud fraction for a given LTS. This suggests that the response of the thermodynamic constraint for C_l to increasing CO_2 concentration is a robust part of the climate change.

The second finding partly coincides with conclusions in Dessler (2010). The cloud response to radiative forcing shows up primarily on the fast time scale in our experiments and is distinct from the cloud response to natural climate variability. This implies that the ENSO-related C_l variability cannot be used to constrain the C_l response to climate change. At the same time, there might be confusion about the time scale of these responses. Namely, Dessler (2010) discussed the observational constraint on short-term variability, which corresponds to the natural variability which appeared on the long time scale in our $4\times CO_2$ experiments (Fig. 5). This apparently opposite result could arise from the experimental design of the abrupt CO_2 increase. Since the time scale of the fast response depends not only on the system's inertia (cf. Held et al. 2010) but also on the time scale of the change in the radiative forcing, the fast response identified in this study appears on much longer time scales in realistic 20th century and future scenario runs (Watanabe et al. 2011b).

On one hand, the above arguments may be somewhat discouraging because they suggest that the radiatively forced C_l response can hardly be constrained from the observed natural variability. On the other hand, the response of the thermodynamic condition to the abrupt CO_2 increase, i.e. ΔLTS, which shows a large similarity among the models both in terms of sign and horizontal distribution (Fig. 10), is encouraging to the modelling groups. This suggests that the LTS change is not crucially dependent on the details of cloud representation such as sub-cloud layer and coupling between cloud physics and turbulence. Yet, the magnitude of ΔLTS was largely different among the eight models analysed here, so that further studies are needed to deepen our understanding of the LTS change under global warming.

In contrast to the robust thermodynamic change discussed above, the change in the vertical structure of low clouds for a given LTS is complex and is still divergent among the models (Fig. 9). Even though the thermodynamic contribution to ΔC_l (first term in Eq. 3b) is positive in all the models, any cloud structure change due to other processes (second term in Eq. 3b) would have a positive contribution to ΔC_l in some models but negative in others. It is not clear what processes are responsible for the latter, and a systematic approach, not simply comparing the GCM outputs, is desirable to pursue this question. For example, a single column model derived from a GCM and therefore including all the physical processes represented therein will be a useful tool to examine the cloud response to a prescribed large-scale forcing (Zhang and Bretherton 2008). At the same time, we anticipate that the ongoing second phase of CFMIP based on newer versions of GCMs will provide another set of multi-model ensemble. It is thus imperative to analyse and compare the cloud response between the two CFMIP ensembles when they become available. We will attempt to contribute to such activity, and also plan to generate another model ensemble based on a hybrid version of MIROC3.2 and MIROC5 in which individual parameterization schemes can be interchangeable. The results will be reported elsewhere.

Acknowledgments. We are grateful to Takuji Kubota of JAXA for assistance in using the satellite cloud data. This work was supported by the Innovative Program of Climate Change Projection for the 21^{st} Century ('Kakushin' program) from MEXT, Japan. The computation was carried out on the Earth Simulator and NEC SX at NIES.

REFERENCES

Andrews T, Forster PM, Gregory JM (2009) Surface energy perspective on climate change. J Clim 22: 2557-2570

Caldwell P, Bretherton CS (2009) Response of a subtropical stratoculumus-capped mixed layer to climate and aerosol changes. J Clim 22: 20-38

Clement AC, Burgman RB, Norris JR (2009) Observational and model evidence for positive low-level cloud feedback. Science 325: 460-464

Dessler AE (2010) A determination of the cloud feedback from climate variations over the past decade. Science 330: 1523-1527

Forster PMF, Gregory JM (2006) The climate sensitivity and its components diagnosed from Earth radiation budget data. J Clim 19: 39-52

Gregory J, Webb M (2008) Tropospheric adjustment induces a cloud component in CO_2 forcing. J Clim 21: 58-71

Hagihara Y, Okamoto H, Yoshida R (2010) Development of a combined CloudSat/CALIPSO cloud mask to show global cloud distribution. J Geophys Res 115: D00H33, doi:10.1029/2009JD012344

Hasumi H (2006) CCSR Ocean Component Model (COCO) Version 4.0. CCSR Report, 25, 103pp [available at http://www.ccsr.u-tokyo.ac.jp/~hasumi/COCO/index.html]

Held IM, Winton M, Takahashi K, Delworth T, Zeng F, Vallis GK (2010) Probing the fast and slow components of global warming by returning abruptly to preindustrial forcing. J Clim 23: 2418-2427

Ishii M, Kimoto M, Sakamoto K, Iwasaki S (2006) Steric sea level changes estimated from historical ocean subsurface temperature and salinity analyses. J Oceanogr 62: 155-170

K-1 model developers (2004) K-1 coupled model (MIROC) description. In: Hasumi H, Emori S (edn) K-1 technical report. Center for Climate System Research, University of Tokyo, 34pp [available at http://www.ccsr.u-tokyo.ac.jp/~agcmadm/]

Klein SA, Hartmann DL (1993) The seasonal cycle of low stratiform clouds. J Clim 6: 1587–1606

Larson K, Hartmann DL, Klein SA (1999) The role of clouds, water vapor, circulation, and boundary layer structure in the sensitivity of the tropical climate. J Clim 12: 2359-2374

Marchand R, Mace GG, Ackerman T, Stephens G (2008) Hydrometeor detection using CloudSat—An Earth-orbiting 94-GHz cloud radar. J Atmos Oceanic Technol 25: 519-533

Medeiros B, Hall A, Stevens B (2005) What controls the mean depth of the PBL? J Clim 18: 3157-3172

Medeiros B, Stevens B (2011) Revealing differences in GCM representations of low cloud. Clim Dyn 36: 385-399

Miller RL (1997) Tropical thermostats and low cloud cover. J Clim 10: 409-440

Murphy DM, Solomon S, Portman RW, Rosenlof KH, Forster PM, Wong T (2009) An observationally based energy balance for the Earth since 1950. J Geophys Res 114: D17107

Okamoto H, Sato K, Hagihara Y (2010) Global analysis of ice microphysics from CloudSat and CALIPSO: Incorporation of specular reflection in lidar signals. J Geophys Res 115: D22209, doi:10.1029/2009JD013383

Onogi K, Tsutsui J, Koide H, Sakamoto M, Kobayashi S, Hatsushika H, Matsumoto T, Yamazaki N, Kamahori H, Takahashi K, Kadokura S, Wada K, Kato K, Oyama R, Ose T, Mannoji N, Taira R (2007) The JRA-25 Reanalysis. J Meteor Soc Japan 85:

369-432

Reichler T, Kim J (2008) How well do coupled models simulate Today's climate? Bull Amer Met Soc 89: 303-311

Ringer MA, McAvaney B, Andronova N, Buja L, Esch M, Ingram W, Li B, Quaas J, Roeckner E, Senior C, Soden BJ Volodin E, Webb MJ, Williams KD (2006) Global mean cloud feedbacks in idealized climate change experiments. Geophys Res Lett 33: L07718

Rossow WB, Schiffer RA (1999) Advances in understanding clouds from ISCCP. Bull Amer Meteor Soc 80: 2261-2287

Solomon S, Qin D, Manning M, Marquis M, Averyt K, Tignor MMB, Miller Jr HL, Chen Z, Eds (2007) *Climate Change 2007: The Physical Sciences Basis.* Cambridge University Press, Cambridge, UK and New York, USA, 996 pp

Su H, Jiang JH, Vane DG, Stephens GL (2008) Observed vertical structure of tropical oceanic clouds sorted in large-scale regimes. Geophys Res Lett 35. Doi: 10.1029/2008GL035888

Tsushima Y, Emori S, Ogura T, Kimoto M, Webb MJ, Williams KD, Ringer MA, Soden BJ, Li B, Andronova N (2006) Importance of the mixed-phase cloud distribution in the control climate for assessing the response of clouds to carbon dioxide increase: A multi-model study. Clim Dyn 27: 113-126

Uppala SM, KÅllberg PW, Simmons AJ, Andrae U, Da Costa Bechtold V, Fiorino M, Gibson JK, Haseler J, Hernandez A, Kelly GA, Li X, Onogi K, Saarinen S, Sokka N, Allan RP, Andersson E, Arpe K, Balmaseda MA, Beljaars ACM, Van De Berg L, Bidlot J, Bormann N, Caires S, Chevallier F, Dethof A, Dragosavac M, Fisher M, Fuentes M, Hagemann S, Hólm E, Hoskins BJ, Isaksen L, Janssen PAEM, Jenne R, Mcnally AP, Mahfouf JF, Morcrette JJ, Rayner NA, Saunders RW, Simon P, Sterl A, Trenberth KE, Untch A, Vasiljevic D, Viterbo P, Woollen J (2005) The ERA-40 re-analysis. Quarterly Journal of the Royal Meteorological Society 131: 2961-3012

Vecchi GA, Soden BJ, Wittenberg AT, Held IM, Leetmaa A, Harrison MJ (2006) Weakening of tropical Pacific atmospheric circulation due to anthropogenic forcing. Nature 441: doi:10.1038/nature04744

Wang Y, Xie SP, Xu H, Wang B (2004) Regional model simulations of marine boundary layer clouds over the Southeast Pacific off South America. Part I: Control experiment. Mon Wea Rev 132: 274-296

Watanabe M, Suzuki T, O'ishi R, Komuro Y, Watanabe S, Emori S, Takemura T, Chikira M, Ogura T, Sekiguchi M, Takata K, Yamazaki D, Yokohata T, Nozawa T, Hasumi H, Tatebe H, Kimoto M (2010) Improved climate simulation by MIROC5: Mean states, variability, and climate sensitivity. J Clim 23: 6312-6335

Watanabe M, Chikira M, Imada Y, Kimoto M (2011a) Convective control of ENSO simulated in MIROC. J Clim 24: 543-562

Watanabe M, Shiogama H, Yokohata T, Ogura T, Yoshimori M, Emori S, Kimoto M (2011b) Constraints to the tropical low-cloud trends in historical climate simulations. Atmos Sci Lett 12. doi:10.1002/asl.337

Webb MJ, Senior CA, Sexton DMH, Ingram WJ, Williams KD, Ringer MA, McAvaney BJ, Colman R, Soden BJ, Gudgel R, Knutson T, Emori S, Ogura T, Tsushima Y, Andronova N, Li B, Musat I, Bony S, Taylor, KE (2006) On the contribution of local feedback mechanisms to the range of climate sensitivity in two GCM ensembles. Clim Dyn 27: 17–38

Williams KD, Ringer MA, Senior CA, Webb MJ, McAvaney BJ, Andronova N, Bony S, Dufresne JL, Emori S, Gudgel R, Knutson T, Li B, Lo K, Musat I, Wegner J, Slingo A, Mitchell JFB (2006) Evaluation of a component of the cloud response to climate change in an Intercomparison of climate models. Clim Dyn 29: 145-165

Williams KD, Tselioudis G (2007) GCM Intercomparison of global cloud regimes: present-day evaluation and climate change response. Clim Dyn 29: 231-250

Winker DM, Vaughan MA, Omar A, Hu Y, Powell KA, Liu Z, Hunt WH, Young SA (2009) Overview of the CALIPSO mission and CALIOP data processing algorithms. J Atmos Oceanic Technol 26: 2310-2323

Wiyant M, Bretherton CS, Bacmeister JT, Kiehl JT, Held IM, Zhao M, Klein SA, Soden BJ (2006) A comparison of tropical cloud properties and responses in GCMs using mid-tropospheric vertical velocity. Clim Dyn 27: 261-279

Wood R, Bretherton CS (2006) On the relationship between stratiform low cloud cover and lower-tropospheric stability. J Clim 19: 6425-6432

Zhang M, Bretherton C (2008) Mechanisms of low cloud-climate feedback in idealized single-column simulations with the Community Atmospheric Model, version 3 (CAM3). J Clim 21: 4859-4878

Zhang T, Stevens B, Medeiros B, Ghil M (2009) Low-cloud fraction, lower-tropospheric stability, and large-scale divergence. J Clim 12: 4827-4844

FIGURE CAPTIONS

Fig. 1a-f Local correlation maps of monthly anomalies: **a** C_l and ω_{500} in observations, **b** C_l and LTS in observations, **c-f** same as **a-b** but for 150 y control runs of MIROC3.2 and MIROC5, respectively. The observed C_l data are derived from ISCCP, and both ω_{500} and LTS are calculated from the JRA reanalysis for 1984-2007.

Fig. 2a-f Heterogeneous regression maps of the monthly SST (K) and C_l (%) anomalies associated with the leading SVD between them: **a-b** observations for the period from July 1983 to June 2005 based on Ishii et al. (2006) SST and the ISCCP cloud data, **c-d** observations from June 2006 to November 2008 based on NOAA OISST and CALIPSO, **e-f** 150 y control run of MIROC3.2, and **g-h** 150 y control run of MIROC5. The values of squared covariance fraction and correlation between the corresponding expansion coefficients are shown at the top of each panel.

Fig. 3a-f Scatter plot of the monthly tropical-mean C_l anomaly (%) against the Niño 3 SST anomaly (K): **a** NOAA OISST and CALIPSO C_l data, **b-c** 150 y control runs of MIROC3.2 and MIROC5, respectively. The regression slope and correlation coefficient are also shown. **d-f** Contribution of dynamic (blue) and thermodynamic (red) components to the C_l anomaly as revealed by the scatter plot against the reconstructed C_l (denoted as $\tilde{C}_l$) anomaly corresponding to **a-c**.

Fig. 4a-d Differences in annual-mean fields between the $4xCO_2$ and control runs (Δ): **a,c** regression of the annual-mean ΔSAT (K K^{-1}) on ΔSAT_g in the 10-member ensemble of MIROC3.2 and the 6-member ensemble of MIROC5, **b,d** scatter plot of the global-mean oceanic ΔC_l (%) against ΔSAT_g in MIROC3.2 and MIROC5.

Blue triangles are the ensemble-means from the 20 y integration whereas red crosses denote the values from a single 150 y run.

Fig. 5 Same as Fig. 4**b,d** but for the tropical-mean ΔC_l (%) against ΔSST (K) in the Niño 3 region. Blue triangles are the annual- and ensemble-averages from the 20 y integration whereas yellow stars indicate the values at the first month. Green crosses, red circles, and thick lines denote the annual- and decadal-mean values and the regression slope for the single 150 y run. The background dashed lines are the slopes for the intrinsic variability shown in Fig. 3**b,c**.

Fig. 6 Adjustment components of the response in the 20y ensemble: **a** ΔZ_{PBL} (m) in MIROC3.2, **b** ΔZ_{PBL} in MIROC5, **c** ΔQ (W m^{-2}) in MIROC3.2, **d** ΔQ in MIROC5. White contours in **a-b** indicate climatological-mean Z_{PBL} in the control run.

Fig. 7 Feedback components of the response in the 20y ensemble: **a-b** ΔC_l (% K^{-1}) in MIROC3.2 and MIROC5, respectively, **c-d** $\Delta\omega_{500}$ (hPa dy^{-1} K^{-1}), **e-f** ΔLTS (K K^{-1}), and **g-h** ΔSST (K K^{-1}). The solid and dashed contours in **c-d** indicate the climatological-mean ω_{500} in the control run (+20 and -20 hPa dy^{-1}), and the contours in **e-f** denote the mean LTS of 15 K in the control run.

Fig. 8a-d Low-cloud regime diagrams: **a-b** C_l composites (%) with respect to ω_{500} (hPa dy^{-1}) and LTS (K) in MIROC3.2, **c-d** same as **a-b** but for MIROC5. Blue (red) curves indicate the composite average in the control (4×CO_2) run, and the shading denotes one std dev. The PDF in the control run (4×CO_2) is also shown by the blue (red) curve at the bottom.

Fig. 9a-i Regime composite of the cloud fraction in the lower troposphere over the tropical oceans as sorted by LTS, together with its PDF: **a** CloudSAT/CALIPSO from June 2006 to May 2007, **b** MIROC3.2, **c** MIROC5, **d-i** CFMIP1 models, all from control runs. In **b-i**, contours indicate the difference between the control and either 4xCO_2 or 2xCO_2 runs, and blue (red) curves in the bottom panels are the PDF for the control (4xCO2 or 2xCO2) run. The grey shading in the PDF gives the definition of stable regime.

Fig. 10a-h Difference in the occurrence frequency of stable regime, Δf_s, between the control and increased CO_2 runs: **a** MIROC3.2, **b** MIROC5, **c-h** CFMIP1 models. The grey contours indicate f_s = 90% in the control run. The values of Δf_s in **a-b** have been divided by factor two for comparing with the other panels based on 2×CO_2 runs. The threshold for f_s is indicated in Fig. 9.

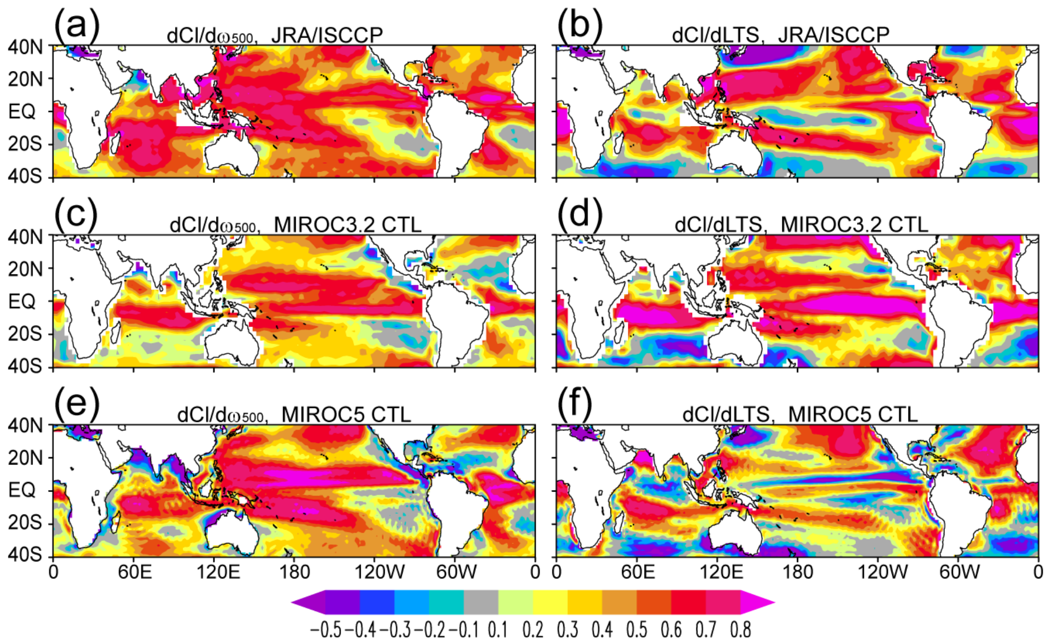

Fig. 1a-f Local correlation maps of monthly anomalies: **a** C_l and ω_{500} in observations, **b** C_l and LTS in observations, **c-f** same as **a-b** but for 150 y control runs of MIROC3.2 and MIROC5, respectively. The observed C_l data are derived from ISCCP, and both ω_{500} and LTS are calculated from the JRA reanalysis for 1984-2007.

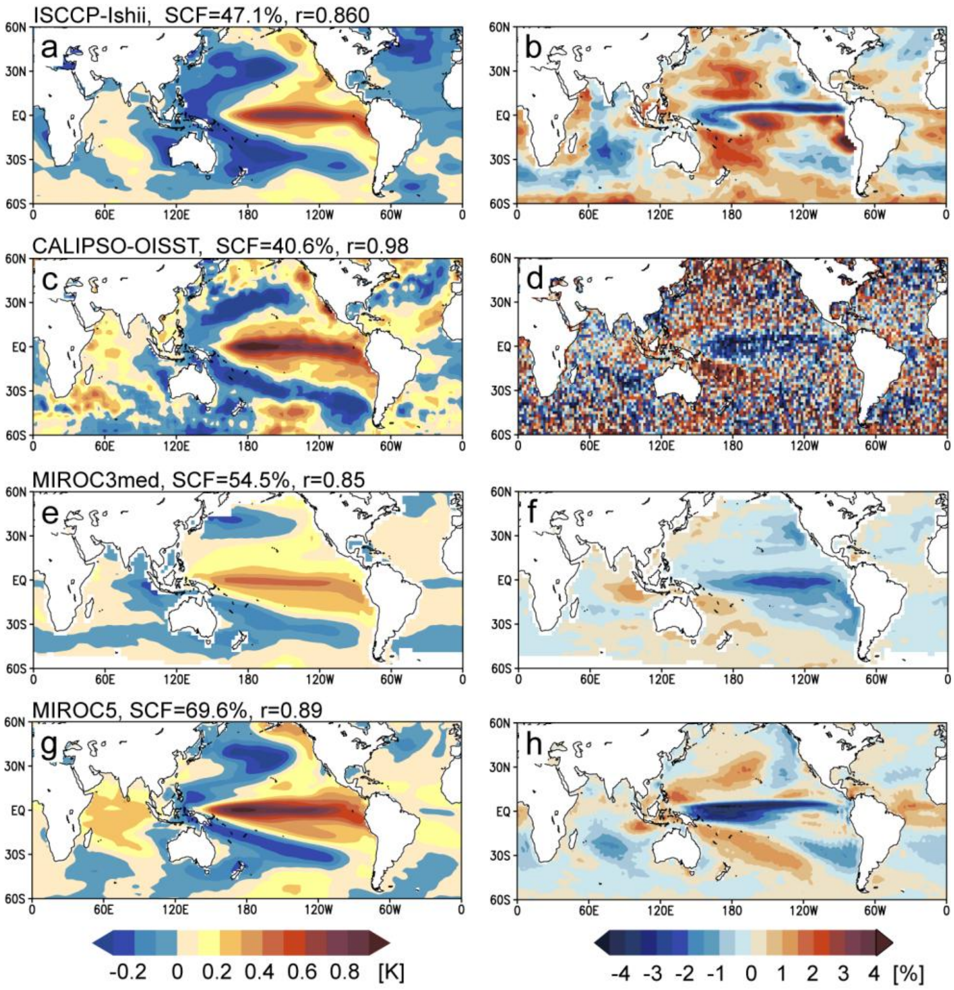

Fig. 2a-f Heterogeneous regression maps of the monthly SST (K) and C_l (%) anomalies associated with the leading SVD between them: **a-b** observations for the period from July 1983 to June 2005 based on Ishii et al. (2006) SST and the ISCCP cloud data, **c-d** observations from June 2006 to November 2008 based on NOAA OISST and CALIPSO, **e-f** 150 y control run of MIROC3.2, and **g-h** 150 y control run of MIROC5. The values of squared covariance fraction and correlation between the corresponding expansion coefficients are shown at the top of each panel.

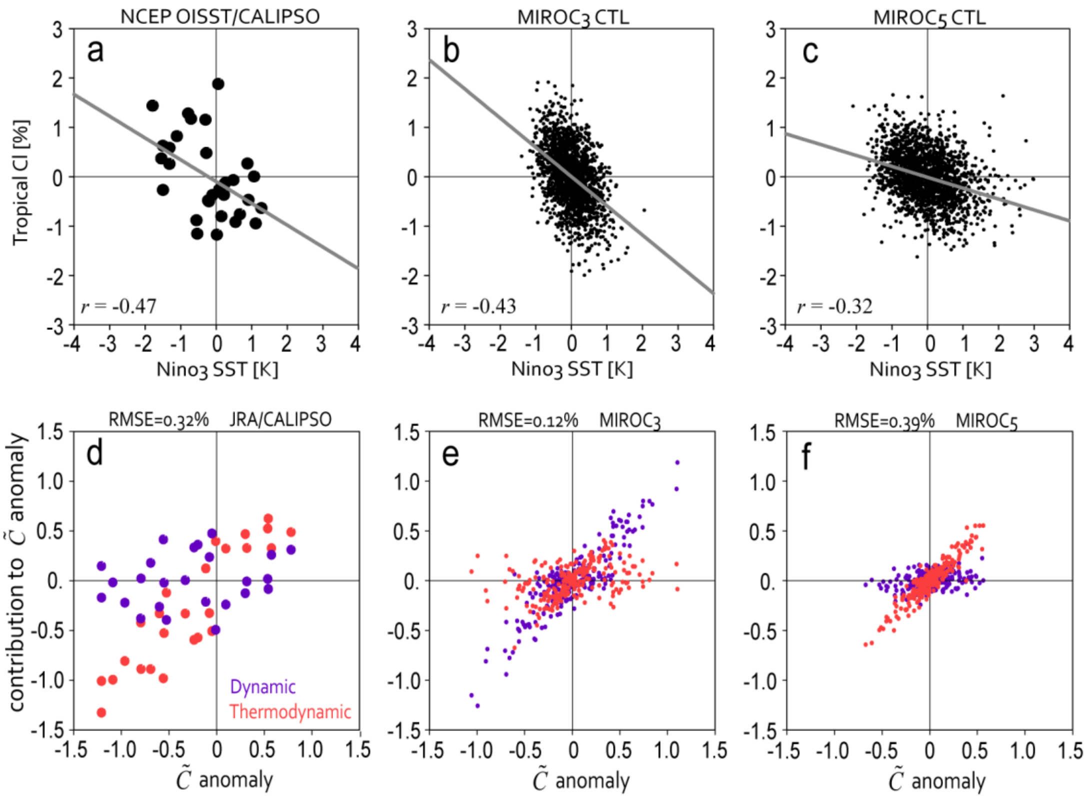

Fig. 3a-f Scatter plot of the monthly tropical-mean C_l anomaly (%) against the Niño 3 SST anomaly (K): **a** NOAA OISST and CALIPSO C_l data, **b-c** 150 y control runs of MIROC3.2 and MIROC5, respectively. The regression slope and correlation coefficient are also shown. **d-f** Contribution of dynamic (blue) and thermodynamic (red) components to the C_l anomaly as revealed by the scatter plot against the reconstructed C_l anomaly corresponding to **a-c**.

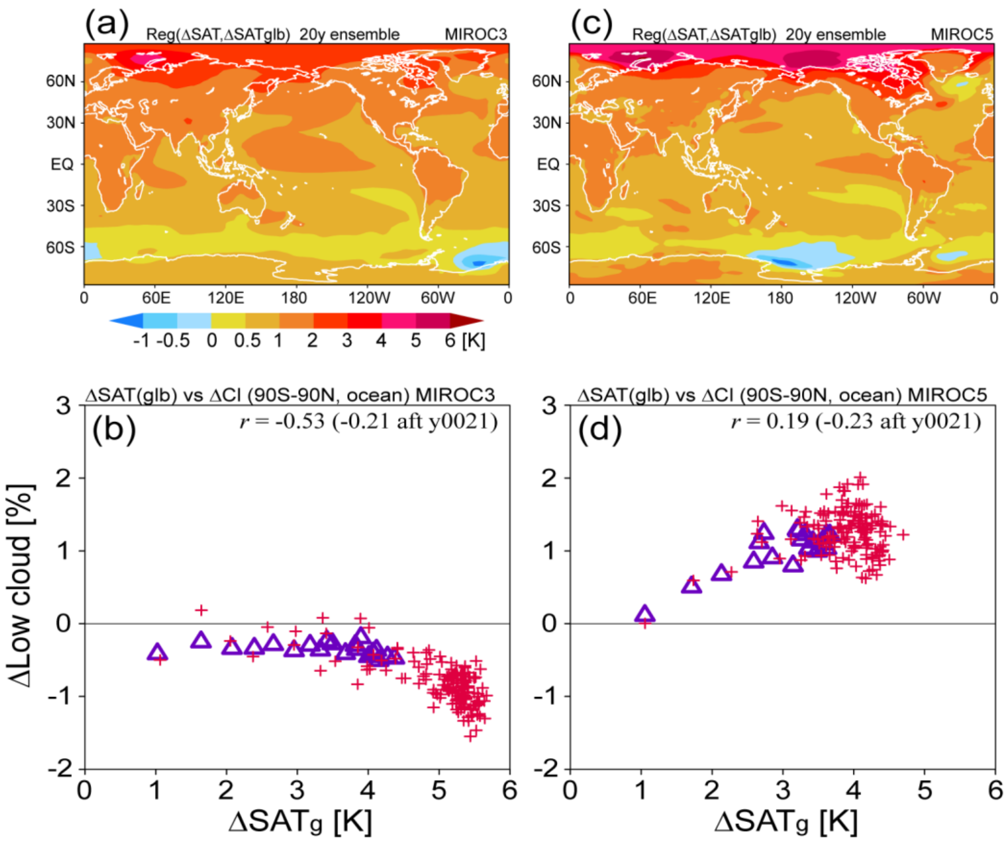

Fig. 4a-d Differences in annual-mean fields between the $4xCO_2$ and control runs (Δ): **a,c** regression of the annual-mean ΔSAT ($K\ K^{-1}$) on ΔSAT_g in the 10-member ensemble of MIROC3.2 and the 6-member ensemble of MIROC5, **b,d** scatter plot of the global-mean oceanic ΔC_l (%) against ΔSAT_g in MIROC3.2 and MIROC5. Blue triangles are the ensemble-means from the 20 y integration whereas red crosses denote the values from a single 150 y run.

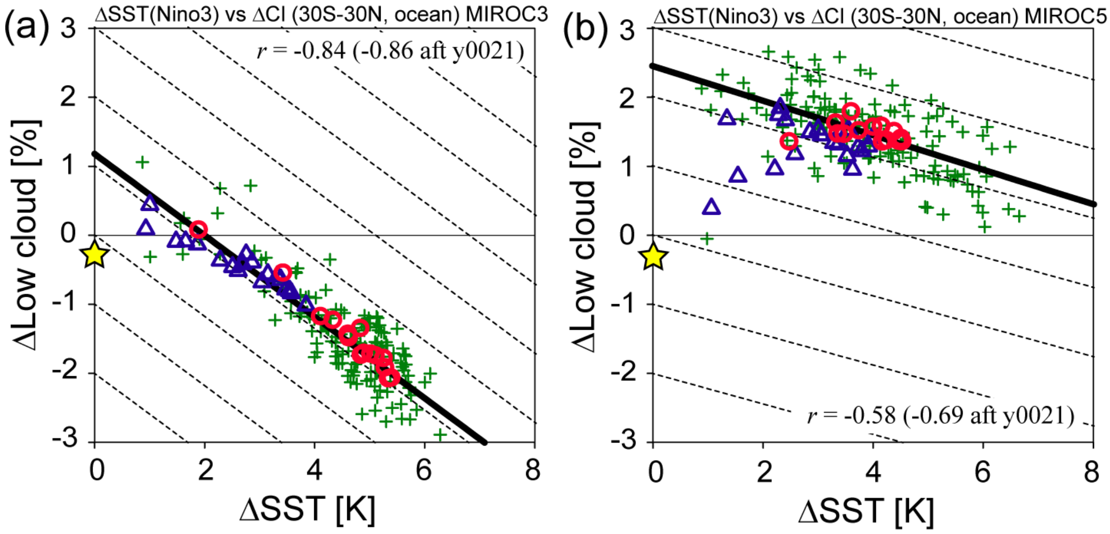

Fig. 5 Same as Fig. 4**b,d** but for the tropical-mean ΔC_l (%) against ΔSST (K) in the Niño 3 region. Blue triangles are the annual- and ensemble-averages from the 20 y integration whereas yellow stars indicate the values at the first month. Green crosses, red circles, and thick lines denote the annual- and decadal-mean values and the regression slope for the single 150 y run. The background dashed lines are the slopes for the intrinsic variability shown in Fig. 3**b,c**.

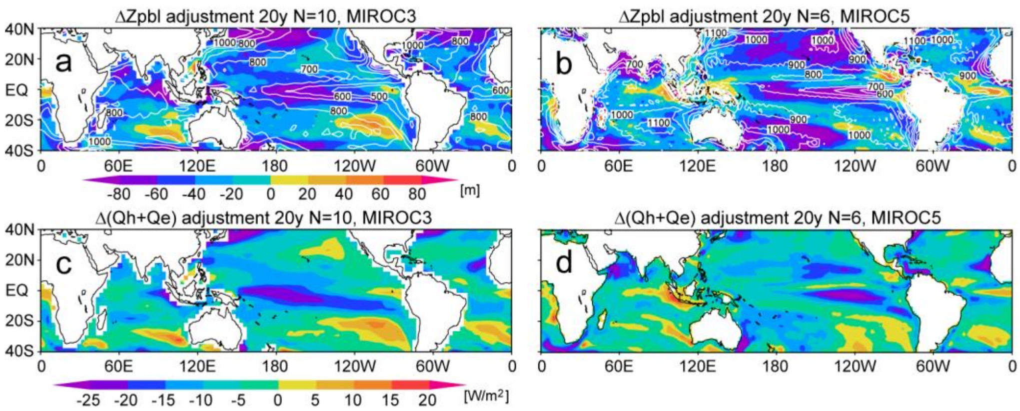

Fig. 6 Adjustment components of the response in the 20y ensemble: **a** ΔZ_{PBL} (m) in MIROC3.2, **b** ΔZ_{PBL} in MIROC5, **c** ΔQ (W m^{-2}) in MIROC3.2, **d** ΔQ in MIROC5. White contours in **a-b** indicate climatological-mean Z_{PBL} in the control run.

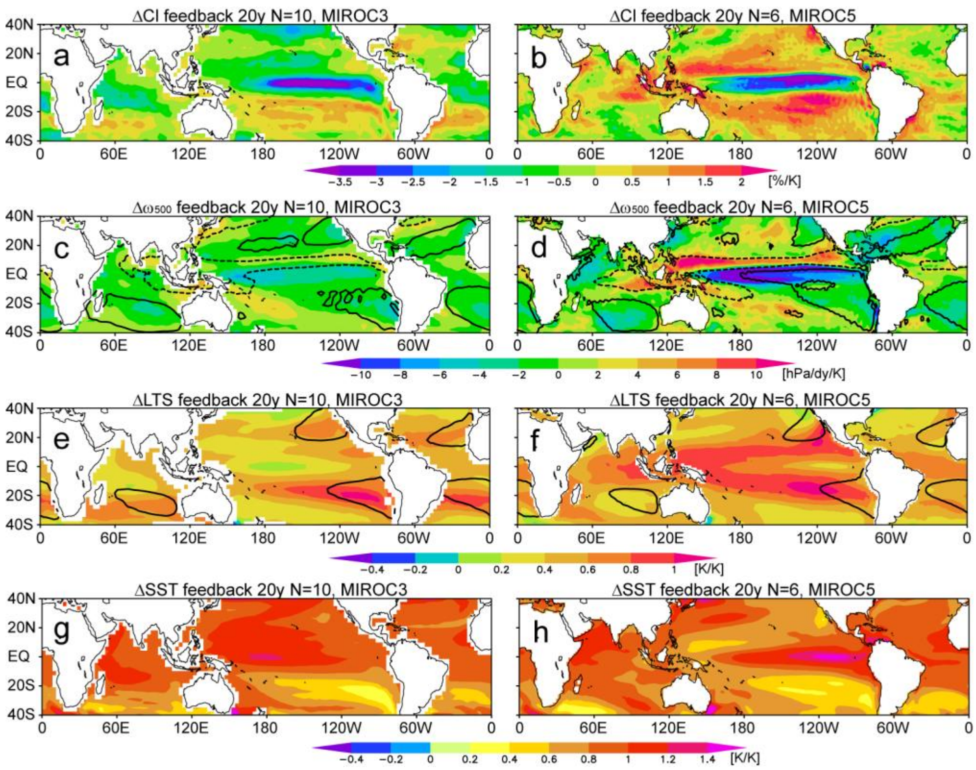

Fig. 7 Feedback components of the response in the 20y ensemble: **a-b** ΔC_l (% K^{-1}) in MIROC3.2 and MIROC5, respectively, **c-d** $\Delta\omega_{500}$ (hPa dy^{-1} K^{-1}), **e-f** ΔLTS (K K^{-1}), and **g-h** ΔSST (K K^{-1}). The solid and dashed contours in **c-d** indicate the climatological-mean ω_{500} in the control run (+20 and -20 hPa dy^{-1}), and the contours in **e-f** denote the mean LTS of 15 K in the control run.

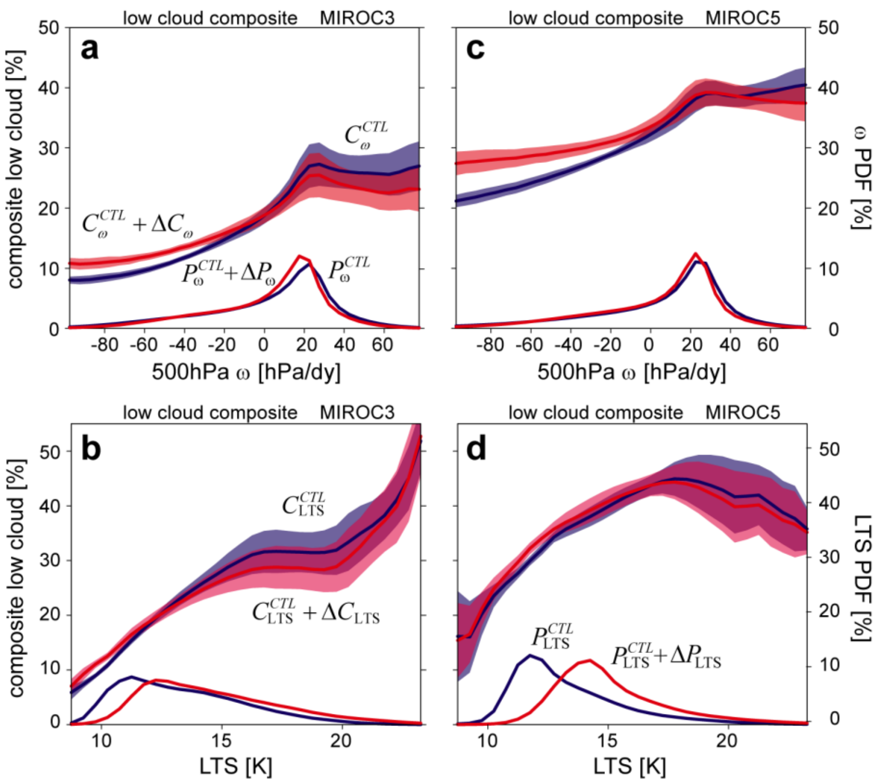

Fig. 8a-d Low-cloud regime diagrams: **a-b** C_l composites (%) with respect to ω_{500} (hPa dy^{-1}) and LTS (K) in MIROC3.2, **c-d** same as **a-b** but for MIROC5. Blue (red) curves indicate the composite average in the control (4×CO_2) run, and the shading denotes one std dev. The PDF in the control run (4×CO_2) is also shown by the blue (red) curve at the bottom.

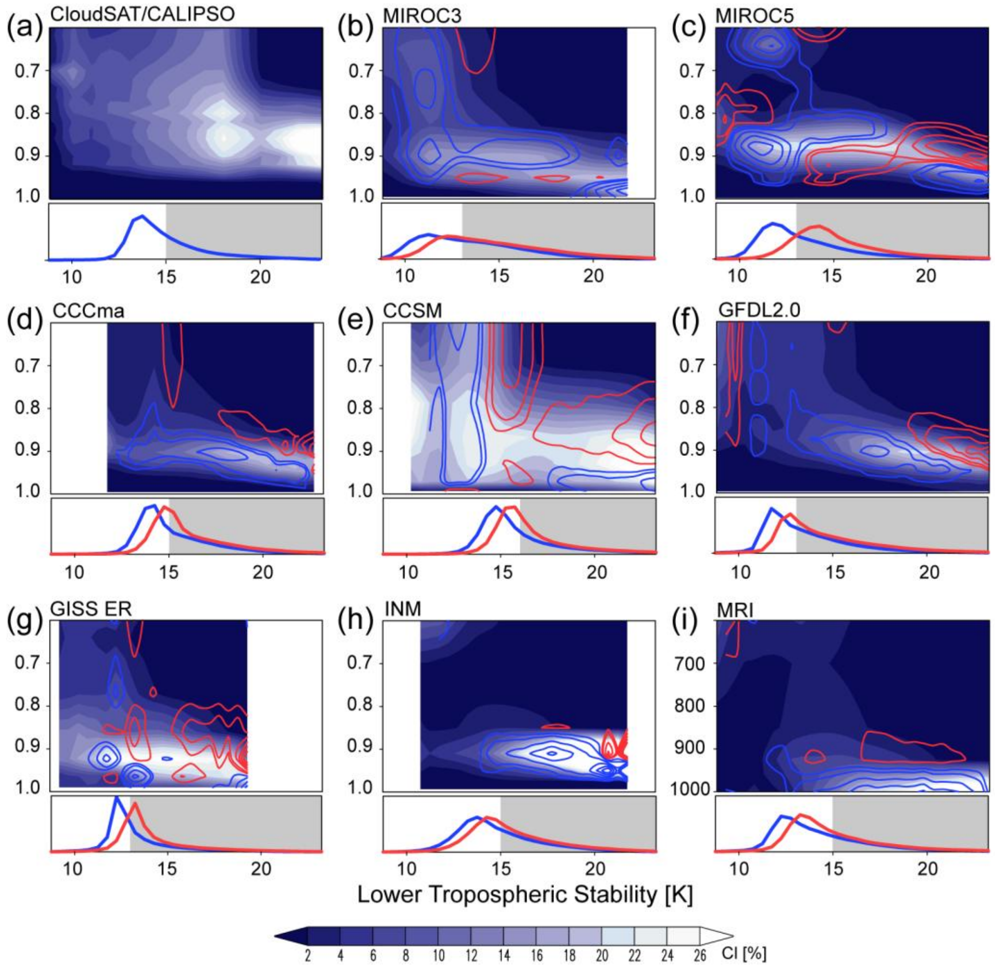

Fig. 9a-i Regime composite of the cloud fraction in the lower troposphere over the tropical oceans as sorted by LTS, together with its PDF: **a** CloudSAT/CALIPSO from June 2006 to May 2007, **b** MIROC3.2, **c** MIROC5, **d-i** CFMIP1 models, all from control runs. In **b-i**, contours indicate the difference between the control and either $4xCO_2$ or $2xCO_2$ runs, and blue (red) curves in the bottom panels are the PDF for the control (4xCO2 or 2xCO2) run. The grey shading in the PDF gives the definition of stable regime.

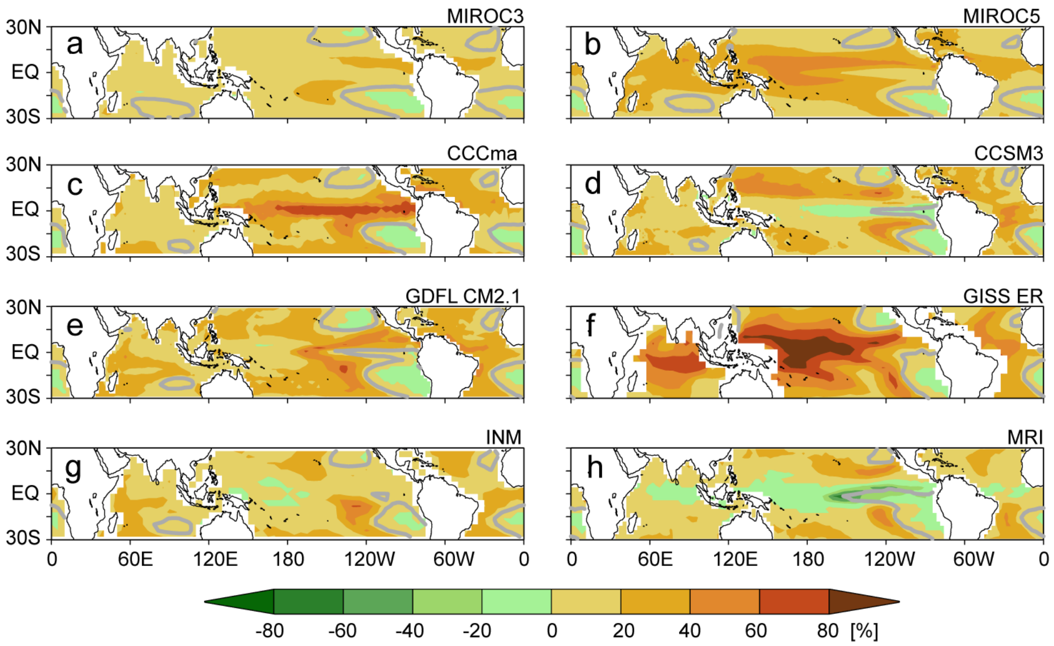

Fig. 10a-h Difference in the occurrence frequency of stable regime, Δf_s, between the control and increased CO_2 runs: **a** MIROC3.2, **b** MIROC5, **c-h** CFMIP1 models. The grey contours indicate f_s = 90% in the control run. The values of Δf_s in **a-b** have been divided by factor two for comparing with the other panels based on $2 \times CO_2$ runs. The threshold for f_s is indicated in Fig. 9.